



Cerium-copper oxides prepared by solution combustion synthesis for total oxidation reactions: From powder catalysts to structured reactors

Marco Piumetti*, Samir Bensaid, Tahrizi Andana, Nunzio Russo, Raffaele Pirone, Debora Fino

Department of Applied Science and Technology, Politecnico di Torino, Corso Duca degli Abruzzi 24, 10129 Torino, Italy



ARTICLE INFO

Article history:

Received 29 July 2016

Received in revised form

21 December 2016

Accepted 23 December 2016

Available online 26 December 2016

Keywords:

Cerium-copper oxide catalysts

Catalytic oxidation of CO

Catalytic oxidation of VOC

Soot combustion

Monolithic catalyst

ABSTRACT

A set of cerium-copper oxide catalysts with various Ce/Cu contents was synthesized using the solution combustion synthesis (SCS) technique. Catalytic activities of the prepared materials were tested for the CO oxidation, total oxidation of ethene and soot combustion. As a whole, the best performances in terms of both CO oxidation and ethene total oxidation were achieved for the binary oxide catalysts having Ce/Cu ratio ranging from 0.67 to 1.5. It has been observed that catalysts with CuO_x clusters interacting with CeO₂ are particularly effective for both the oxidation reactions. This confirms that CeO_x and CuO_x domains may cooperate synergistically, leading to higher oxidation activity because of the easier surface reducibility and more abundant structural defects (oxygen vacancies). On the other hand, the soot combustion activity increases as a function of the Ce-content up to 95 at.%. Indeed, the best soot oxidation catalyst exhibits copper highly dispersed into the ceria framework (Ce-O-Cu species), along with an abundant population of Cu⁺ species and H-bonded hydroxyl groups. Finally, the best performing powder catalysts were deposited on Silicon Carbide (SiC)-type monoliths through a novel synthesis and their catalytic activity was confirmed in a laboratory-scale pilot plant reactor. All the prepared catalysts were characterized by physico-chemical techniques, including XRD, FESEM, TEM, N₂ physisorption at -196 °C, H₂-TPR, XPS, FT-IR and micro-Raman spectroscopies.

© 2016 Elsevier B.V. All rights reserved.

1. Introduction

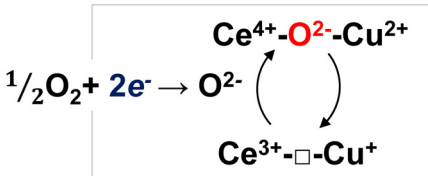
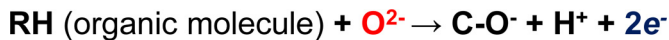
Nowadays, one of the main applications of heterogeneous catalysis concerns protection of the environment via removal of toxic compounds from car exhausts [1]. Catalytic oxidation, in fact, is a widely used technique to reduce engine-out emissions: it is less fuel intensive than thermal oxidation and it is highly versatile, thus allowing waste streams to be treated with different compositions and flow rates [2–4].

It is generally accepted that many oxidative processes, such as the VOC total oxidation [5], soot combustion [6,7] and CO oxidation [8] over ceria-based materials can be kinetically modelled via a Mars–van Krevelen (MvK)-type mechanism [9]. Specifically, the reaction involves alternating reduction-oxidation steps on the catalyst surface with the formation of oxygen vacancies and successive replenishment by gas-phase oxygen [10–12]. Moreover, it

has been well established that the incorporation of metals (e.g. Fe, Cu, Zr, Pr) into the CeO₂ lattice may have a beneficial effect on the structural and electronic properties of the solid catalyst, thus improving the oxidation activity and thermal stability [13–15]. In heterogeneous catalysis, in fact, there are several characteristic examples in which the presence of multi-component catalysts influences the solid-state chemistry, since active phases (and promoters) may interact with each other [16–18]. For instance, the concept of "strong metal support interaction" (SMSI) was first introduced in the late seventies to explain the drastic changes in the chemisorption properties of group VIII noble metals supported on TiO₂ [19,20]. Since then, much effort has been directed to explain the SMSI phenomena, which are not only limited to the interaction between the noble metal and titanium cations but may occur with many multi-component catalysts, such as the ceria-based materials [14], leading to beneficial phenomena (synergies). For instance, a synergistic reaction pathway has been observed with CuO-CeO₂ catalysts effective for CO oxidation: both the CeO₂ and the CuO phases are simultaneously reduced or oxidized with CO or O₂, respectively. A schematization of the redox cycle occurring

* Corresponding author.

E-mail address: marco.piumetti@polito.it (M. Piumetti).



Scheme 1. Redox cycle of the Ce-Cu-O systems.

in Ce-Cu-O systems is shown in **Scheme 1**. The effectiveness of such redox (MvK)-type mechanism for many oxidation reactions is essentially due to the electronic interaction between the CuO and CeO₂ phases, as confirmed by cyclic voltammetry investigations and temperature-programmed reaction studies [21].

As a whole, synergies in oxidation catalysis typically arise through phase-cooperation and spillover effects. Grasselli [22] introduced the concept of “phase-cooperation” for oxidation and ammonoxidation reactions: Two phases (α , β) with different properties, when brought into contact with each other (γ phase) may lead to better catalytic results than those that can be reached by the two phases acting separately and independently from each other. On the other hand, spillover phenomena involve the surface diffusion of active species (e.g. oxygen, hydrogen, etc.) adsorbed on one phase (donor) onto a second phase (acceptor) which does not form the active species under the same conditions [23,24]. When the surface sites are “irrigated” by spillover species, the catalyst significantly improves its chemical reactivity [23–26].

Accordingly, Delmon et al. [27] proposed the “remote-control” concept to explain the fact that a wide number of oxidation catalysts used for industrial processes are multiphasic (e.g. mixed oxide catalysts) and that specific phase compositions lead to synergistic phenomena. In this scenario, Ce-Cu oxide catalysts are particularly interesting for a wide range of oxidation processes because of their high ability to reduce and re-oxidize the overall catalytic reaction. Several studies, in fact, have shown the promising oxidation activity of CeO₂-CuO catalysts for CO oxidation [28–31] and total oxidation of VOCs [32–35].

In the present work, a set of Ce-Cu oxide catalysts with different Ce/Cu contents was synthesized by the solution combustion synthesis (SCS) method, an effective route for the synthesis of metal oxide catalysts. In fact, the exothermicity of the combustion reaction, as well as the extensive gas release during the process, enhances the production of highly crystalline and porous materials in the nanoscale range. Another important aspect of this synthesis procedure is its intrinsic ability to modify the chemical composition of powder catalysts by varying the precursors.

The oxidation activity of the prepared catalysts was tested with three characteristic oxidation reactions: CO oxidation, total oxidation of ethene and soot combustion. Then, the catalysts were characterized by complementary techniques, including XRD, FESEM, TEM, N₂ physisorption at -196°C , H₂-TPR, XPS, FT-IR and micro-Raman spectroscopies.

Finally, the most active powder catalysts were deposited on a Silicon Carbide (SiC)-type monolith through the SCS route and tested in a laboratory-scale pilot plant reactor, using the catalytic oxidation of CO, ethene and soot as test reactions.

2. Experimental

2.1. Catalysts preparation

A set of Ce-Cu oxide catalysts with various Ce-Cu contents (hereafter referred to as Ce_xCu_{1-x} where x indicates the Ce/Cu + Ce

atomic ratio) was synthesized by means of solution combustion synthesis (SCS), in agreement with previous studies [36,37]. The following set of Ce-Cu oxide catalysts was prepared: CeO₂, Ce_{0.95}Cu_{0.05}, Ce_{0.85}Cu_{0.15}, Ce_{0.60}Cu_{0.40}, Ce_{0.40}Cu_{0.60}, Ce_{0.15}Cu_{0.85}, Ce_{0.05}Cu_{0.95} and CuO. The SCS route allows to obtain powder samples (single metal oxides and binary oxides) in the nanoscale size.

In short, proper amounts of Ce(NO₃)₃, Cu(NO₃)₂ and urea (in stoichiometric conditions) were dissolved in 50 ml of deionized water and stirred at room temperature (r.t.) for 30 min. The homogeneous solution was then placed in an oven at 600°C for 20 min. The resultant powder was washed with deionized water to remove impurities and dried at 90°C overnight.

The SCS method was also used to prepare two catalytic monoliths with optimal Ce/Cu ratios. Thus, the chemical compositions of the most effective powder catalysts (namely, Ce_{0.95}Cu_{0.05} and Ce_{0.60}Cu_{0.40}) were considered to prepare the catalytic monoliths on commercial Silicon Carbide (SiC) filters (IBIDEN-180 cpsi; porosity = 0.42; 1.5 × 1.5 × 3 cm length) (namely, Ce_{0.95}Cu_{0.05}-SiC and Ce_{0.60}Cu_{0.40}-SiC). In a typical synthesis, stoichiometric amounts of Ce(NO₃)₃, Cu(NO₃)₂ and urea were dissolved in 50 ml of deionized water and stirred at r.t. for 30 min. The monolith was then dipped into the slurry solution so that the precursors could enter the inner channels. The monolith was then placed in an oven and left at 600°C for 20 min. Finally, the catalytic monolith was cooled at r.t. and any excess powder was removed using compressed air. This procedure was repeated several times in order to obtain a higher amount of the active phase (final amount of active phase loaded onto the monolith = 10 wt.%).

In order to get the catalytic filter for the soot combustion tests, a ceramic paste was used to plug the opposite ends of adjacent channels of the monolith (thus recovering the original filter configuration). The catalytic filter was washed with distilled water and then dried overnight at 90°C . Finally, the filter was dipped in a suspension of soot (Degussa Printex U) in 100 ml heptane (soot loaded onto the monolith = 6 g/l). After dipping, the filter was vigorously shaken and, then, dried at r.t.

2.2. Catalyst characterization

The X-ray diffraction patterns were collected on an X'Pert Philips PW3040 diffractometer using Cu K α radiation (2θ range = 15° – 70° ; step = 0.05° 2θ ; time per step = 0.2 s). The XRD patterns were indexed according to the Powder Data File database (PDF 2000, International Centre of Diffraction Data, Pennsylvania). The average size of the crystallites was determined using the Scherrer formula, $D = 0.9\lambda/b\cos\theta$, where λ is the wavelength of the Cu K α radiation, b is the full width at half maximum (in radians), 0.9 is the shape factor for spherical particles and θ is the angle of the diffraction peaks.

Sample morphology was observed through a field emission scanning electron microscope (FESEM Zeiss MERLIN, Gemini-II column) and transmission electron microscopy (TEM, Jeol JEM 3010 operating at 200 kV). The chemical composition of the samples was determined through EDS analysis (Oxford X-ACT): three different spots with a 10–50 nm diameter were selected in representative zones of the sample, and the average Cu-content was then calculated. Moreover, the Cu-content was verified by inductively coupled plasma atomic emission spectroscopy (ICP-MS) on an ICAP-Q Thermo instrument.

The specific surface area (S_{BET}) and total pore volume (V_p) were measured by N₂ physisorption at -196°C (Micrometrics ASAP 2020) on powders previously outgassed at 200°C for 4 h to remove water and other atmospheric contaminants; S_{BET} was determined according to the Brunaure-Emmett-Teller (BET) method.

H₂-TPR analysis was performed to study the reducibility of the catalysts. Sample pretreatment was conducted prior to analysis by

treating 50 mg of catalyst under air (40 ml min^{-1}) at 150°C for 1 h, followed by cooling with Ar to r.t. H₂-TPR analysis was executed by increasing gradually sample temperature to 750°C with the rate of 5°C min^{-1} under Ar (4.95%-mol H₂ in Ar). The instrument was equipped with thermal conductivity detector (TCD) to recognize the H₂ signal.

XPS (X-ray photoelectron spectroscopy) measurements were performed on an XPS PHI 5000 Versa probe apparatus using a band-pass energy of 187.85 eV, a 45° take off angle and a $100.0 \mu\text{m}$ diameter X-ray spot size. Curve-fits were performed by means of Multipack 9.0 software.

Raman measurements were performed using a Renishaw InVia Raman microscope with laser excitations at 785 nm in backscattering light collection (objective 50x; acquisitions 50; power 3 mW). The O_v/F_{2g} value, representative of the oxygen vacancies density, was calculated as the ratio between the areas of the O_v and F_{2g} Raman peaks obtained by averaging the spectra recorded on 3 different points of the sample. The regions for the integration were selected depending on the Raman shift of the peaks for each catalyst composition and excitation wavelength.

FT-IR spectra were collected on an FT-IR spectrophotometer (Equinox 55, Bruker), equipped with an MCT (Mercury Cadmium Telluride) cryodetector. To remove water and other atmospheric contaminants, wafers were pre-outgassed at 150°C for 1 h before the analysis. Pre-treatments were carried out using a standard vacuum frame in an IR quartz cell quipped with KBr windows.

2.3. Catalytic activity tests

Catalytic activity tests were performed in a quartz U-tube reactor with inner diameter = 4 mm, heated by an electric furnace; temperature was measured by means of a thermocouple placed in the middle of the catalytic bed.

2.3.1. CO oxidation reaction

0.1 g of powdered catalyst was inserted in the reactor. Then, the catalytic bed was pre-treated in He (flow rate = 50 ml min^{-1}) for 1 h at 150°C . The test started by flowing 50 ml min^{-1} gas containing 1000 ppm of CO and 10% O₂ in N₂ into the reactor (GHSV of 19100 h^{-1}). The temperature was then raised by 5°C min^{-1} in the range from 50 to 450°C .

2.3.2. VOC total oxidation reaction

0.1 g of powdered catalyst was pretreated in He (flow rate = 100 ml min^{-1}) for 1 h at 150°C to remove any species adsorbed on the catalyst surface. The gas flow was then switched from He to the reactive mixture: 500 ppm ethene and 10% O₂ were fed with N₂ to the reactor with a gas hourly space velocity (GHSV) of $19,100 \text{ h}^{-1}$. The catalytic reaction was started when the temperature was stable at 100°C . The temperature was then raised by 5°C min^{-1} from 100°C up to 700°C .

2.3.3. Soot oxidation reaction

The catalytic bed was prepared by mixing 5 mg of carbon soot (Printex-U), 45 mg of powdered catalyst and 150 mg of inert silica in “tight” contact conditions, as described elsewhere [6,38]. The test started by flowing 100 ml min^{-1} gas comprising of 50% air and 50% N₂ to the reactor. The temperature increased from 100 to 700°C with 5°C min^{-1} heating rate. The gaseous mixtures were analyzed via CO/CO₂ NDIR analyzers (ABB). Each test was repeated twice to ensure the reproducibility of the obtained results. Temperatures corresponding to 10%, 50%, 90% conversion (denoted as T_{10%}, T_{50%}, T_{90%}, respectively) were taken as indices of the activity of the tested catalysts.

The activity of the catalytic monolith was conducted in a stainless steel reactor heated in a horizontal split tube furnace with

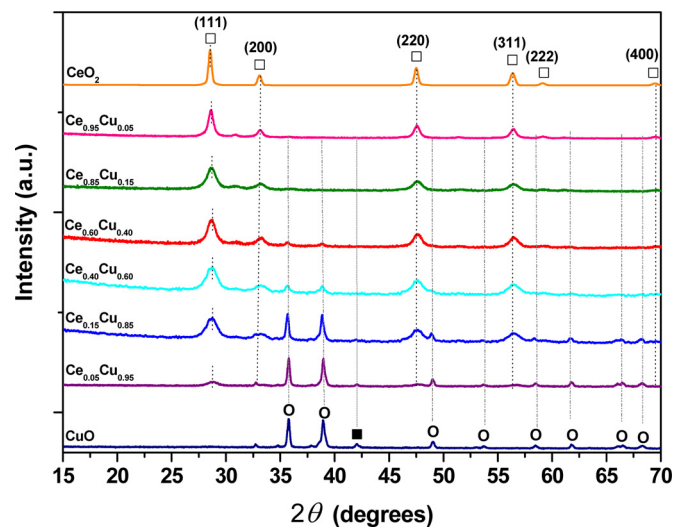


Fig. 1. Powder wide-angle XRD patterns of the powder catalysts (□ = CeO₂; ○ = CuO; ■ = Cu₂O).

Table 1
Textural and structural properties of the powder catalysts.

Catalyst	Crystallite Size ^a (nm)	<i>a</i> ^b (nm)	S _{BET} ^c ($\text{m}^2 \text{ g}^{-1}$)	V _p ^d ($\text{cm}^3 \text{ g}^{-1}$)
CeO ₂	28.6	0.5413	21	0.05
Ce _{0.95} Cu _{0.05}	14.3	0.5394	25	0.06
Ce _{0.85} Cu _{0.15}	9.7	0.5390	24	0.06
Ce _{0.60} Cu _{0.40}	9.1	0.5381	31	0.07
Ce _{0.40} Cu _{0.60}	7.1	0.5373	25	0.06
Ce _{0.15} Cu _{0.85}	6.9	0.5373	16	0.02
Ce _{0.05} Cu _{0.95}	–	0.5373	4	0.01
CuO	–	0.4347*	3	0.01

^a Calculated applying the Scherrer formula.

^b Cell parameter (nm);* calculated for Cu₂O.

^c Specific surface area measured by the BET method.

^d Total pore volume.

a heating length of 60 cm (Fig. S1, Supporting Information). The monolith was sandwiched between two mullite foams in order to optimize the flow distribution. The inlet monolith temperature was controlled by inserting a thermocouple along one side of the central monolith channels. The monolith was pre-treated in He (flow rate = 100 ml min^{-1}) for 2 h at 150°C to remove any species adsorbed on the catalyst surface. The reactor temperature difference, measured between the inlet and the outlet of the reactor in the axial direction, was not very significant ($<10^\circ\text{C}$). The composition of the outlet gases was monitored with the same equipment described above (W/F = 0.03 g l^{-1}).

3. Result and discussion

3.1. Material textural and structural properties

Fig. 1 shows the wide-angle XRD patterns of the samples: the cubic fluorite lattice structure of ceria (Fm3 m symmetry) can be observed for pure CeO₂ and binary oxide catalysts. For the latter samples, reflections of the copper oxide (CuO) phase (35.5° , 38.7° , 48.7° , 53.7° , 58.3° , 61.5° , 66.1° , 66.5° and 68.4°) progressively increase in intensity as a function of the Cu-content (up to 85 at.%). Peaks related to bulk CuO are relevant for the catalysts with the highest Cu-content, namely the Ce_{0.05}Cu_{0.95} and CuO samples. For both the samples, there is a further signal at 42.1° attributed to the presence of the Cu₂O phase [29,34,39]. Crystallite sizes of the samples, as calculated using the Scherrer equation, are reported in **Table 1**. With an increase of the Cu-content (at.%) in the sam-

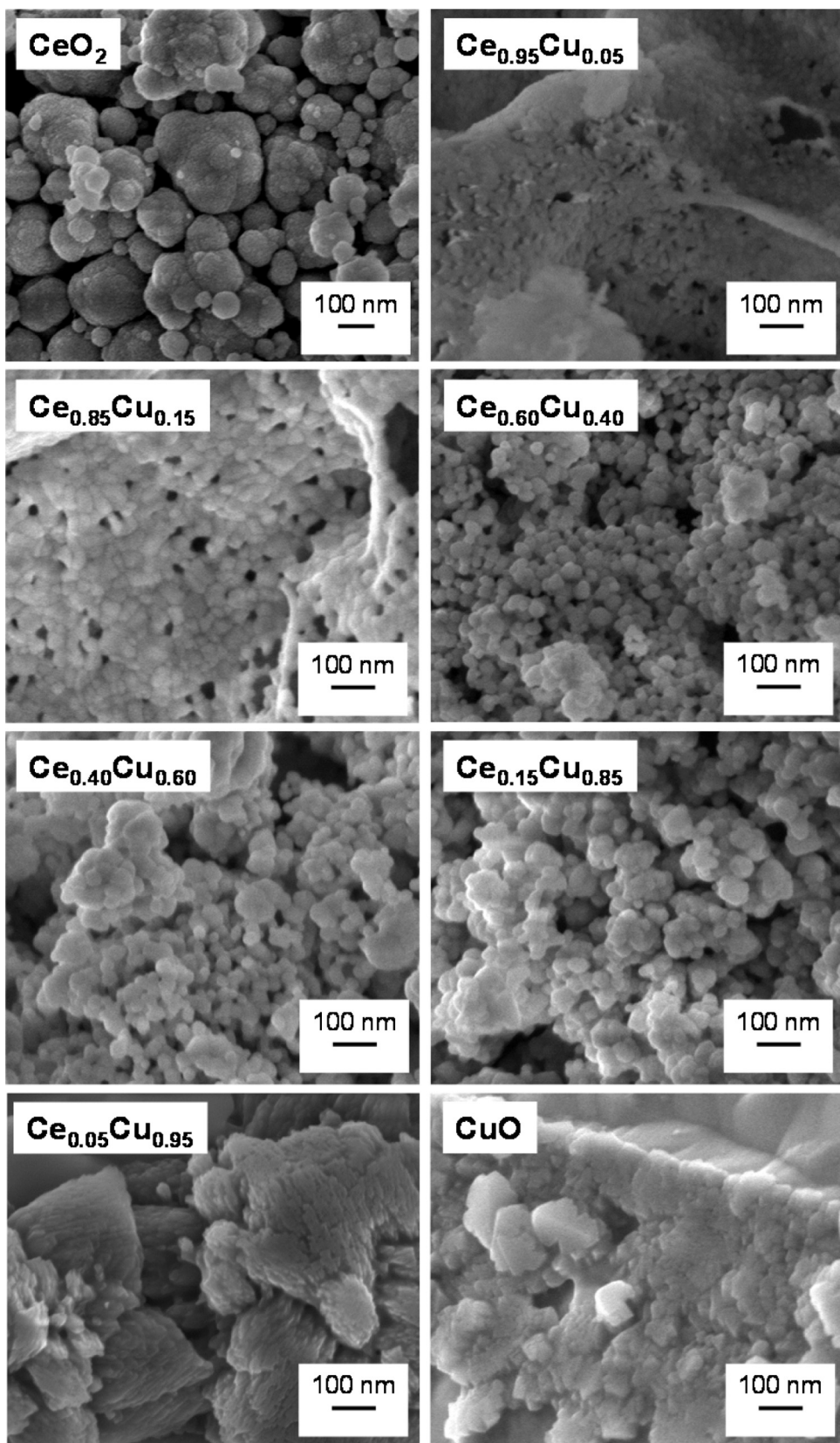


Fig. 2. FESEM images of the powder catalysts.

plexes, the crystallites become smaller, thus confirming that the cell size decreases when Cu^{2+} ions are introduced into the CeO_2 lattice [39,40]. This finding is essentially due to the smaller ionic radius

of Cu^{2+} (0.76 \AA) as compared to either Ce^{4+} (0.91 \AA) or Ce^{3+} ions (1.14 \AA). Thus, pure CeO_2 shows an average particle size of 28.6 nm , whereas progressively smaller particles are obtained for the binary

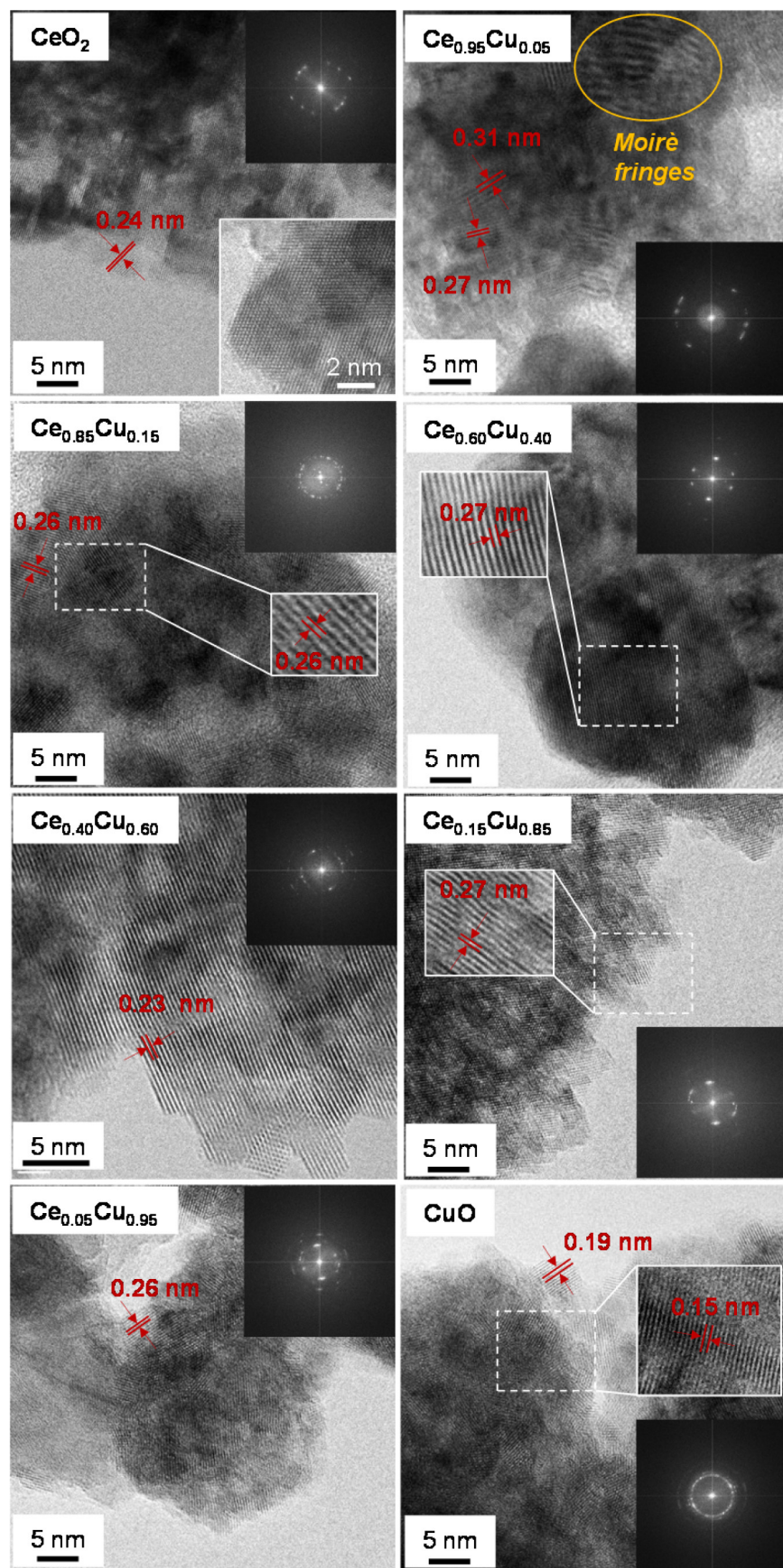


Fig. 3. TEM images of the powder catalysts.

oxide catalysts (up to 6.9 nm for the $\text{Ce}_{0.15}\text{Cu}_{0.85}$). Finally, the CuO and $\text{Ce}_{0.05}\text{Cu}_{0.95}$ samples exhibit lamellar structures, so the Scherrer's equation does not provide reliable data.

Moreover, the cell parameters of the prepared catalysts are summarized in Table 1. As expected, it appears that the incorporation of Cu^{2+} ions into the ceria lattice reduces the cell parameter from 0.5413 nm (pure CeO_2) to 0.5373 nm ($\text{Cu} = 40$ at.%). This finding is in agreement with the lower Cu^{2+} radius with respect to that of the Ce^{4+} . At higher Cu contents, the cell parameter does not vary thus confirming that not all of the Cu species are incorporated into the CeO_2 lattice.

The introduction of copper ions in the ceria lattice suggests the formation of (interfacial) solid solutions for these binary oxides ($\text{Ce}_x\text{Cu}_{1-x}\text{O}_y$ solid solutions) with uniform Cu dispersion. However, the XRD patterns show that copper may be present in different forms, namely as isolated Cu ions in octahedral sites of ceria or copper oxide clusters (CuO_x).

As reported in Table 1, the prepared $\text{Ce}_x\text{Cu}_{1-x}$ samples show similar BET surface areas and pore volumes. The best textural properties are reached for the $\text{Ce}_{0.60}\text{Ce}_{0.40}$ catalyst ($S_{\text{BET}} = 31 \text{ m}^2 \text{ g}^{-1}$; $V_p = 0.07 \text{ cm}^3 \text{ g}^{-1}$), whereas further increases in Cu-contents lead to worse values. The worst textural properties can be observed for the $\text{Ce}_{0.05}\text{Cu}_{0.95}$ sample ($S_{\text{BET}} = 4 \text{ m}^2 \text{ g}^{-1}$ and $V_p = 0.01 \text{ cm}^3 \text{ g}^{-1}$). In agreement with previous studies [33,38], the BET surface areas/total pore volumes for the CeO_2 and CuO samples are $21 \text{ m}^2 \text{ g}^{-1}/0.05 \text{ cm}^3 \text{ g}^{-1}$ and $3 \text{ m}^2 \text{ g}^{-1}/0.01 \text{ cm}^3 \text{ g}^{-1}$, respectively.

Fig. 2 shows the FESEM micrographs of the powder catalysts: agglomerates of primary particles (up to ca. 300 nm) appear for the CeO_2 sample, whereas small clusters with relatively uniform particles (diameters ≈ 30 –50 nm) can be observed for the binary oxides (up to Cu-content = 85 at.%). On the other hand, catalysts with higher Cu-contents (namely, $\text{Ce}_{0.05}\text{Cu}_{0.95}$ and CuO) seem to have smoothed surfaces (lamellar structures with sizes up to few microns) rather than agglomeration of small clusters due to presence of bulk CuO .

TEM images of the samples, and their corresponding Fourier transforms, are shown in Fig. 3. The typical shape of the as-prepared nanocrystals is polyhedral, because of the fluorite structure of ceria. The micrographs generally show multiple nanoparticles displaying lattice fringes whose interplanar distances are compatible with the presence of the fluorite phase in all cases. The most common exposed facets are (200) and (220), corresponding to 0.27 and 0.19 nm interplanar spacing, respectively [14]. No Cu-containing phase was resolved in any of the multiple TEM images taken for these samples in spite of the relatively high copper loading. It appears that the presence of low amounts of Cu into the ceria framework ($\text{Ce}_{0.95}\text{Cu}_{0.05}$ and $\text{Ce}_{0.85}\text{Cu}_{0.15}$) favors the formation of small domains (islands of ca. 10–15 nm), exhibiting different crystalline orientations and Moiré fringes, due to overlapping crystalline planes. On the other hand, larger (ordered) domains occurs for the samples having Ce/Cu ratio ranging from 1.5 to 0.67 ($\text{Ce}_{0.60}\text{Cu}_{0.40}$ and $\text{Ce}_{0.40}\text{Cu}_{0.60}$) compared to the other Ce-Cu oxide catalysts. Finally, the CuO sample exhibit small domains (ca. 5 nm in size) with different crystalline orientations.

3.2. Reducibility and surface properties

The surface reducibility of the materials was studied through the temperature-programmed reduction (TPR) measurements. According to the literature, hydrogen temperature-programmed reduction (H_2 -TPR) offers valuable indications on the reducibility of ceria-based materials [14]. Fig. 4A shows the H_2 -TPR profiles of CeO_2 , CuO and binary oxide catalysts. Pure CeO_2 exhibits a wide peak centred at 475 °C, attributed to the surface reduction of ceria [38,41], while the reduction of bulk CeO_2 occurs above 900 °C (data

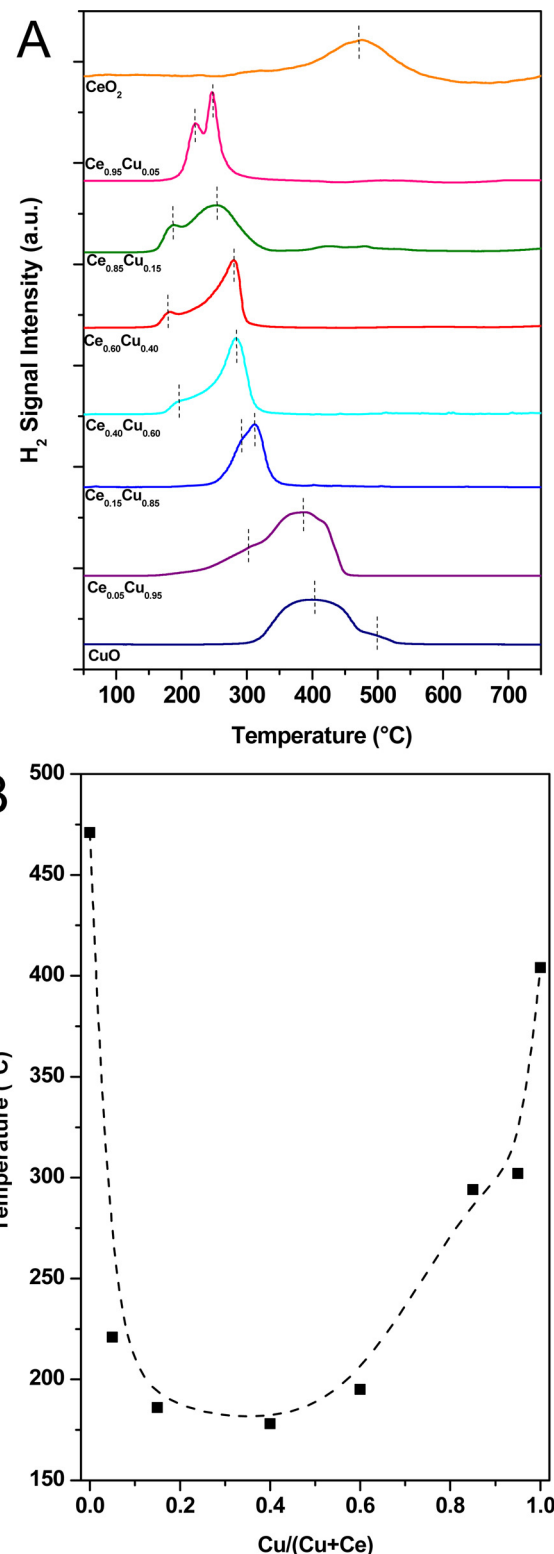


Fig. 4. H_2 -TPR profiles (Section A) and trend of the low-temperature reduction peaks (Section B) of the powder catalysts.

not reported for the sake of brevity). Conversely, pure CuO shows a broad reduction signal above 300 °C, in agreement with the literature [29].

Noteworthy, the reduction of binary oxide catalysts takes place at lower temperatures than those observed for either CeO_2 or CuO .

Moreover, several overlapping peaks appear in the 150–450 °C range, thus rendering the TPR profiles rather complex.

Few copper ions are sufficient to enhance the surface reducibility, as observed for the Ce_{0.95}Cu_{0.05} sample.

Thus, the presence of copper in the CeO₂ structure seems to promote the surface reducibility of ceria-based catalysts, as observed for the Ce_{0.95}Cu_{0.05} sample. The latter, indeed, shows the reduction peaks at 220 and 248 °C, attributed to highly dispersed (isolated or oligomeric) Cu²⁺ ions into the ceria lattice. Thus, Ce-O-Cu species strongly interacting via the SMSI appear in the Ce_{0.95}Cu_{0.05} sample, in agreement with previous studies (Pirone et al. [41]). Similarly, small CuO_x clusters interacting with CeO₂ can be easily reduced at lower temperatures (in the 150–199 °C range), as shown for the Ce_{0.85}Cu_{0.15} and Ce_{0.60}Cu_{0.40} samples [29,33,34,41].

The peaks at higher temperatures (200–400 °C) reflect the reduction of CuO_x clusters well dispersed in the ceria. Reduction peaks in this temperature range occur for the prepared binary oxides and their position shifts to higher temperatures as the Cu-content increases; indeed, the smaller the CuO particles, the easier they are to reduce. Finally, the peaks above 400 °C are attributable to the reduction of bulk CuO [29,33,41–45].

The trend of the low-temperature reduction peak shows that the coexistence of CeO_x and CuO_x domains promote the surface reducibility and then the lowest reduction temperature peak appear for the Ce_{0.60}Cu_{0.40} catalyst (Fig. 4B). Quantitative analysis of TPR runs (Table 2) shows that the H₂-consumption progressively increases with the Cu-content, thus confirming the beneficial role of copper towards the reducibility of ceria-based catalysts. Actually, not only the whole copper species are reduced in the TPR tests, as revealed by a H₂/Cu ratio not less than 1, but also a surplus of H₂-uptake is measured with respect to the only Cu reduction. This means that ceria is reduced in the range of lower temperatures, even lower than the temperatures of surface CeO₂ reduction. Such an effect is evident also in a quantitative way: by estimating the amount of Ce reduced from Ce⁴⁺ to Ce³⁺, assuming that all copper species are reduced, it seems evident that this amount reaches a maximum at around Ce/Cu ≈ 1 (Table 2).

For the Ce_{0.95}Cu_{0.05} the amount of H₂ consumed is higher than the theoretical value (H₂/Cu = 3.0), according to the complete reduction of Cu²⁺ → Cu. This confirms that the surface oxygen bound to ceria can also be reduced in the temperature range of 400–500 °C, as a consequence of the CeO₂ strongly polarized by interaction with vicinal Cu atoms. A similar H₂-uptake, although with lower extent, can be observed for the Ce_{0.85}Cu_{0.15} sample (H₂/Cu = 2.2). Then, CuO_x clusters interacting with ceria (particularly abundant on the Ce_{0.60}Cu_{0.40} and Ce_{0.40}Cu_{0.60} samples) give rise to reduction peaks in the 200–400 °C range, whereas larger CuO_x occur for samples with higher Cu-contents (namely, Ce_{0.15}Cu_{0.85} and Ce_{0.05}Cu_{0.95}).

Fig. 5 shows the XPS spectra in the O (1s), Ce (3d), Cu (2p) core level regions along with the Cu (LMM) Auger spectra. The O (1s) spectra (Section A) report peaks which can be readily assigned to either chemisorbed oxygen (O_α-species) or lattice oxygen (O_β-species). Specifically, the peaks at 527.4–528.9 eV and 529.2–530.3 eV can be ascribed to O_β species (lattice O²⁻) of the Ce-O and Cu-O bonds, respectively, whereas the signals at 531.0–531.6 eV are related to surface oxygens (i.e. O₂²⁻, O⁻, OH⁻, CO₃²⁻) [38,46–48]. Interestingly, two types of O_β species can be observed for the samples with Cu-contents up to 40 at.%, whereas for samples with higher Cu-loadings more electrophilic oxygens occur, as reported in Table S3.

The Ce (3d) core-level spectra (Section B) show the “v” and “u” peaks corresponding to the 3d_{5/2} and 3d_{3/2} states, respectively. The doublets (v₀, u₀), (v₂, u₂), and (v₃, u₃) are assigned to the various states of Ce⁴⁺ ions, whereas the doublet (v₁, u₁) reflects the Ce³⁺

species [38]. Thus, the presence of Ce³⁺ and Ce⁴⁺ species has been estimated for each sample, through the Ce 3d curve-fittings (Table S4).

As summarized in Table S5, the relative abundance of Ce³⁺ species is ca. 29% for pure CeO₂, while it falls in the 6–18% range for the Ce-Cu oxide catalysts. Conversely, the Ce_{0.05}Cu_{0.95} sample does not exhibit the doublet (v₁ and u₁) and so the abundance of Ce³⁺ ions is negligible for this sample.

Fig. 5C shows the Cu (2p) spectra for the Cu-containing samples: peaks at 930.1–934.8 eV and 948.9–953.6 eV are assigned to Cu 2p_{3/2} and Cu 2p_{1/2} transitions, respectively [46–48]. Both peaks are quite broad and exhibit signals due to Cu²⁺ (933.2–934.8 eV and 952.7–953.6 eV for 2p_{3/2} and 2p_{1/2}, respectively) and Cu⁺ (930.1–933.4 eV and 948.9–952.1 eV for 2p_{3/2} and 2p_{1/2}, respectively) states. The corresponding satellites occur in the 937.0–944.0 eV (Cu⁺ 2p_{3/2}), 947.0–948.3 eV (Cu⁺ 2p_{1/2}) and 959.6–962.5 eV (Cu²⁺ 2p_{1/2}) ranges [29,46–48]. In the spectrum of CuO sample, the main signal can be deconvoluted into two smaller peaks representing two different species of Cu²⁺. The former species (933.6 eV), denoted as Cu²⁺ (I), are ascribed to Cu²⁺ bounded with lattice O²⁻ anions (Cu-O); the latter (935.1 eV), denoted as Cu²⁺ (II), reflect surface Cu²⁺ bounded with other oxygen species, i.e. hydroxyls or carbonates [49]. From the spectra deconvolution (Table S5), the CuO sample comprises lattice Cu²⁺ (I) (≈59%) and Cu²⁺ (II) species (≈41%), while Cu⁺ is hardly detected. Conversely, binary oxides with lower Cu contents exhibit more abundant Cu⁺ species, marked by a peak in the 932–933 eV range [47], in agreement with previous studies [29,50]. Specifically, in the Ce_{0.15}Cu_{0.85} sample, Cu⁺ species begins to appear albeit little (≈6%) but the remarkable increase in Cu⁺ ions is observed for the Ce_{0.6}Cu_{0.4} sample, where the Cu⁺ concentration is around 27%. Thus, the highest concentration of Cu⁺ species (≈69%) can be observed for the Ce_{0.95}Cu_{0.05} sample.

These findings confirm that samples with Cu/CuO_x species well dispersed into the CeO₂ lattice exhibit a richer population of Cu⁺ species, likely due to the substitution at the interface of the two oxide phases (strong interactions between Cu/CuO_x and CeO₂), since both the Ce⁴⁺ and Cu⁺ radii are comparable in size [50].

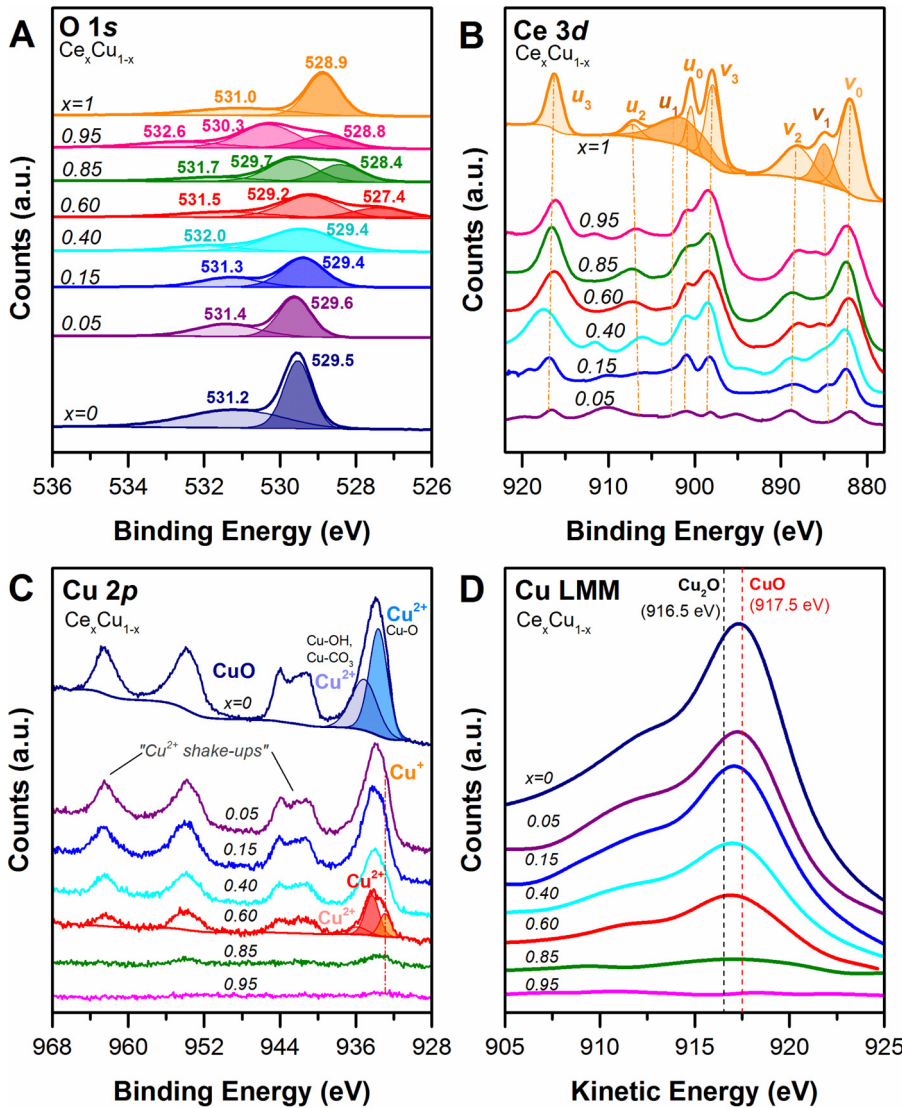
Finally, Fig. 5D exhibits Cu LMM Auger spectra for all Cu-containing samples, since the peaks of Cu⁺ and Cu⁰⁰ in 2p_{3/2} region are nearly indistinguishable due to an extremely small difference in peak position (BE). From the LMM spectra, indeed, we can estimate more easily the most dominant species. The Auger peaks are mostly centered at kinetic energy (KE) range of 917.0–917.5 eV which is the characteristic of CuO phase (or indirectly speaking “Cu²⁺”) [47]. Peak broadening in most spectra, especially those of samples with higher Cu-contents, may explain the presence of bonds of Cu²⁺ with weaker oxygen species (e.g. OH⁻ and CO₃²⁻) as the peak of pure CuO is rather sharp. Moreover, the spectra show a peak “shoulder” in the 910–915 eV range attributed to CuO.

In samples with Cu/Ce ≈ 1 at./at.%, i.e. Ce_{0.6}Cu_{0.4} (shown by the red curve), the broadening may be due to the presence of Cu⁺ as its peak normally appears at lower KE (916.5 eV) [47,51]. The Ce_{0.85}Cu_{0.15} sample eventually confirms the presence of Cu⁺ as its peak, albeit feeble in intensity, is visibly shifted to lower KE, near the standard value for Cu₂O. Conversely, the peak of Cu⁰⁰ (metallic) in an LMM Auger spectrum is normally encountered at 918.7 eV, whereas the current peaks shown in Fig. 5D appear at lower KE. In addition, the characteristic of Cu⁰⁰ LMM Auger spectrum, with a broad signal in the 919–920 eV range, is not found in the current spectra.

Raman spectroscopy was used to investigate the abundance of oxygen defects in the prepared samples. The transport of oxygen in the ceria-based materials results in the creation of intrinsic point defects. According to the literature, indeed, the relative intensity ratio between the defect band (I_{Ov}) and the F_{2g} signal (I_{F2g}) of the

Table 2H₂ consumption (mmol H₂ g_{cat}⁻¹) measured by the TPR analysis.

Catalyst	Cu ^g at.%	Total H ₂ -uptake	H ₂ -uptake 150–199 °C	H ₂ -uptake 200–399 °C	H ₂ -uptake 400–500 °C	H ₂ -uptake >500 °C	H ₂ /Cu	Red ^f (%)
CeO ₂	–	0.52	–	–	–	0.52 ^e	–	6.7
Ce _{0.95} Cu _{0.05}	4.9	0.88	–	0.33, 0.55 ^b	–	–	3.0	7.7
Ce _{0.85} Cu _{0.15}	15.7	2.2	0.35 ^a	1.85 ^c	–	–	2.2	17.4
Ce _{0.60} Cu _{0.40}	38.9	3.9	0.40 ^a	3.50 ^c	–	–	1.4	18.0
Ce _{0.40} Cu _{0.60}	58.1	6.1	–	2.1, 4.0 ^c	–	–	1.2	24.6
Ce _{0.15} Cu _{0.85}	85.1	9.3	–	9.3 ^c	–	–	1.02	8.5
Ce _{0.05} Cu _{0.95}	94.1	11.1	–	4.1, 7.0 ^c	–	–	1.002	2.8
CuO	100	12.6	–	–	11.8, 0.78 ^d	–	1.0	–

^a small CuO_x clusters.^b highly dispersed Cu²⁺ ions in the CeO₂ framework.^c CuO_x interacting with CeO₂.^d CuO.^e bulk CeO₂.^f reduced Ce (Ce³⁺ %), calculated as Ce⁴⁺ species reduced to Ce³⁺.^g measured by IPC-MS analysis.**Fig. 5.** XPS spectra of the powder catalysts in the O (1s) (Section A), Ce (3d) (Section B) and Cu (3d) (Section C) core level regions along with Cu (LMM) Auger spectra (Section D).

fluorite phase can be a valuable indicator of the O_v-density [13,52]. Thus, the ratio between the areas of the O_v and F_{2g} peaks is the most appropriate way to compare the population of oxygen vacancies in different solids: the higher the O_v/F_{2g} area ratio value the higher the amount of oxygen vacancies.

All the Raman spectra of the catalysts are reported in Fig. 6A. As a whole, both the CeO₂ and binary oxide catalysts exhibit the signal related to the symmetric breathing mode (F_{2g}) of oxygen atoms around Ce⁴⁺ ions at 463 cm⁻¹ (characteristic peak of the fluorite structure) and the peak at 605 cm⁻¹ assigned to Frenkel-type

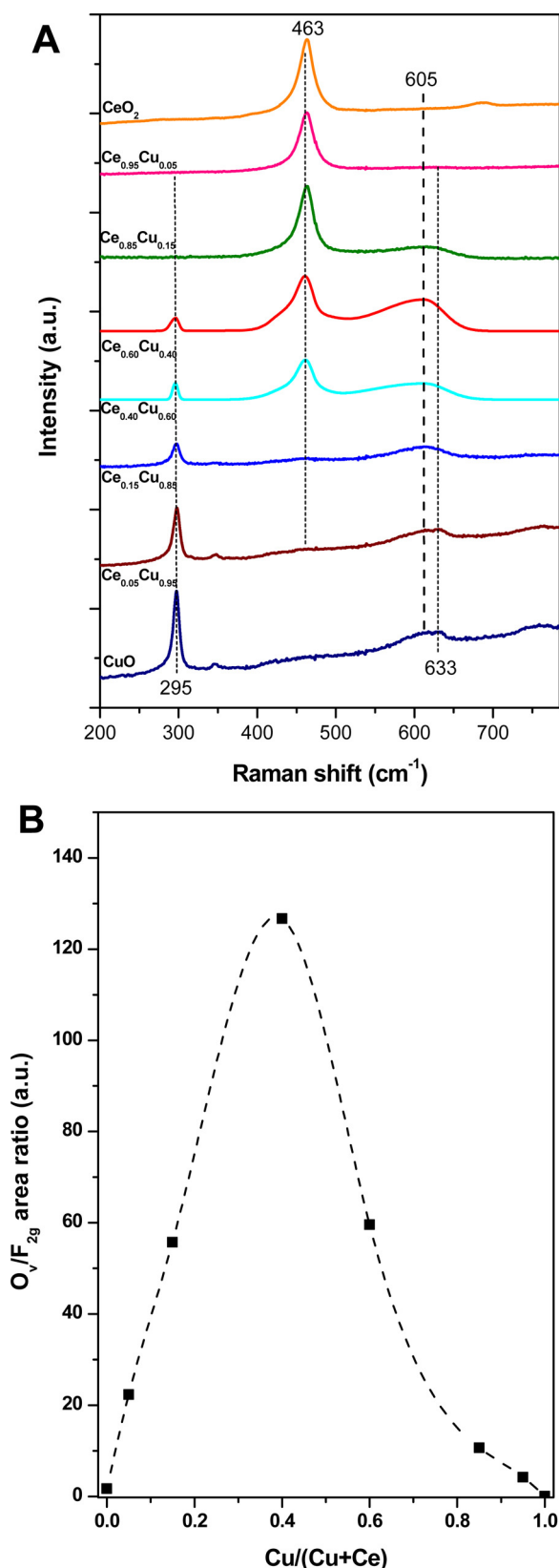


Fig. 6. Micro-Raman spectra, in the 200–750 cm⁻¹ range, recorded at ambient conditions for the powder catalysts (left) along their O_v/F_{2g} area ratios (right).

anion defects in the solid [13]. In the latter case, an oxygen ion occupies an interstitial position, leaving a vacancy at its original lattice site. Fig. 6B shows the trend of the O_v/F_{2g} values: it appears that the addition of Cu species into the ceria framework promotes the formation of structural defects and the highest O_v/F_{2g} value can be observed for the Ce_{0.60}Cu_{0.40} sample. On the other hand, the formation of a CuO bulk phase in the binary oxides progressively increases as a function of the Cu-content (peaks at 295 and 633 cm⁻¹), in agreement with the results of bulk CuO [53,54].

Fig. 7 shows the FT-IR spectra of the samples outgassed at 150 °C. All the reported spectra were normalized to unit specific weight to allow a comparison to be made. In the O–H stretching region (Section A) the following bands can be observed: isolated hydroxyls (3710–3700 cm⁻¹), bridging hydroxyls (3660–3640 cm⁻¹), multiple bonded hydroxyls (3550–3500 cm⁻¹) and hydrogen bridging hydroxyls (broad band at 3400–3100 cm⁻¹) [55,56].

Fig. 7A shows O–H stretching bands, although with different intensities: pure CeO₂ and binary oxides with higher Ce-contents (Ce in the 60–95 at.% range) exhibit an abundant population of isolated, bridged hydroxyls and multiple bonded OH groups. In particular, the Ce_{0.95}Cu_{0.05} sample shows an intense signal in the 3600–3100 cm⁻¹ range related to the presence of multiple bonded hydroxyls. This finding appears in agreement with the presence of more reactive (and accessible) redox sites, as a consequence of the SMSI effect. On the other hand, at higher Cu-contents, as well as for the CuO sample, only hydrogen bridging OH groups appear at the surface (i.e. Cu²⁺–OH in agreement with XPS results).

At lower wavenumbers (Fig. 7B), all spectra show signals in the 1800–1000 cm⁻¹ range, readily assigned to C–O stretching and bending modes of carbonate and formate species. When acting as an electrophile, CO₂ reacts with oxygen defects or hydroxide species giving rise to formates (1560 cm⁻¹) and polidentate carbonates [57], which are particularly abundant on the CeO₂ sample (bands at 1470, 1365, 1056 cm⁻¹) [55,58,59]. On the other hand, only few carbonate-carboxylate compounds appear for CuO and binary oxide catalysts, as a consequence of their easier surface dehydroxylation, thus suggesting a good accessibility of the active (redox) centres during the catalytic reaction.

3.3. Catalytic activity tests

The catalytic activity of the powder catalysts was tested with three oxidation reactions, namely the CO oxidation, ethene total oxidation and soot combustion. The latter are fundamental for environmental catalysis (i.e. in VOCs abatement, exhaust gas aftertreatment, etc.) and are prototypical reactions for the catalyst surface characterization [6,8,13,60–64]. Catalytic performances of the powder catalysts are summarized in Table 4.

Similarly, the catalytic monoliths were tested in a laboratory-scale pilot plant reactor.

3.3.1. CO oxidation

The catalytic behaviour towards the CO oxidation was tested in the 50–450 °C temperature range. Fig. 8A shows the CO conversion to CO₂ as function of the reaction temperature achieved for the prepared catalysts along with the uncatalyzed reaction. As expected, all the catalysts exhibit positive CO conversion trends for an increasing reaction temperature and total oxidation of CO is reached at about 120 °C for the Ce_{0.60}Cu_{0.40}. The latter catalyst exhibited the best results in terms of T_{10%–50%–90%} values (79, 99 and 117 °C, respectively) and specific CO oxidation rate (=11.96 mmol m⁻² h⁻¹ at 90 °C) (Table 4A). Moreover, the trend of the specific oxidation rates (Fig. 8B) shows the beneficial effect of the coexistence of CeO_x and CuO_x species and the highest activity arises for the Ce_{0.60}Cu_{0.40} catalyst. In other words, the interaction between CuO_x clusters and CeO₂ appears a key factor for promoting CO oxidation, most likely

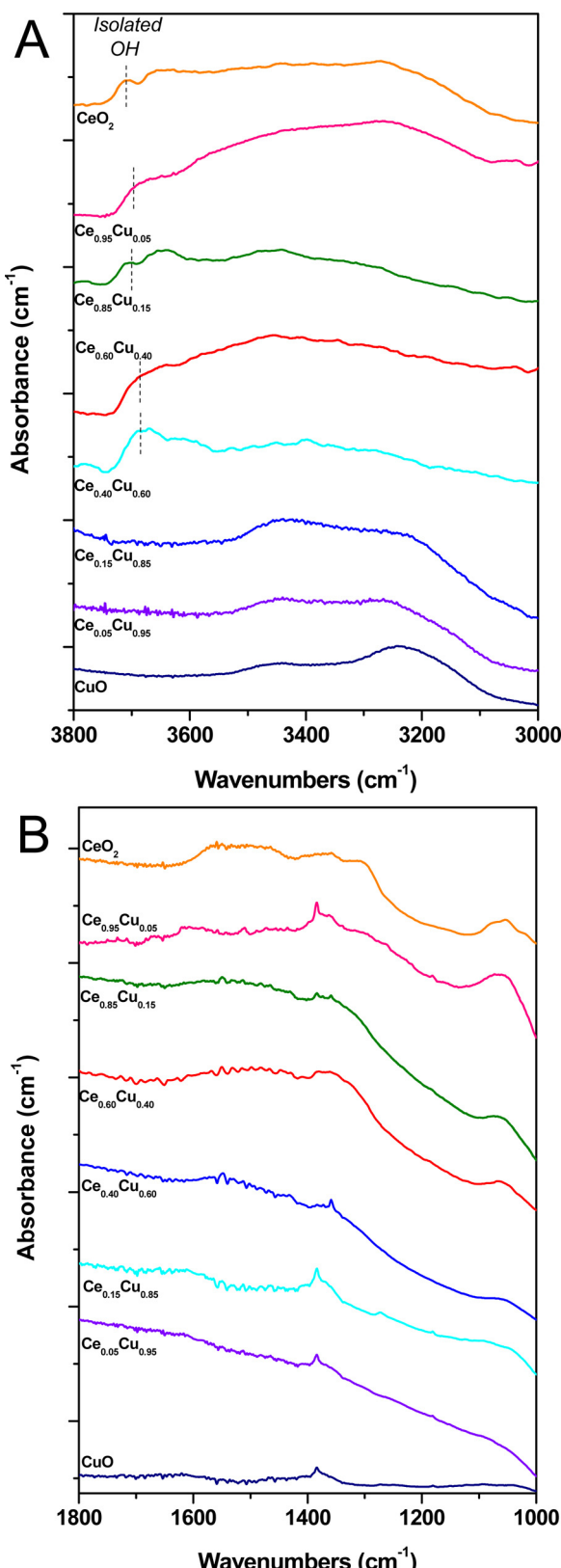


Fig. 7. FT-IR spectra, in the 3800–3000 cm⁻¹ (Section A) and 1800–1000 cm⁻¹ (Section B) of the samples outgassed at 150 °C.

Table 3

Schematic summary of some literature reports on the main implications of Cu-ceria interactions for catalytic applications.

Catalytic applications	Hypothesis/Experimental evidences	References
CO oxidation	Coexistence of Ce ⁴⁺ /Ce ³⁺ and Cu ²⁺ /Cu ⁺ redox pairs High reducibility Abundance of surface oxygen defects	[66–75]
VOC oxidation	High O ₂ dissociation ability Coexistence of Ce ⁴⁺ /Ce ³⁺ and Cu ²⁺ /Cu ⁺ redox pairs High reducibility Abundance of surface oxygen defects	[66,76–81]
Soot combustion	Abundant population of surface-oxygen species High reducibility	[6,66,82–86]

Table 4

Catalytic performances of the powder catalysts for the CO oxidation (Section A), ethene total oxidation (Section B) and soot combustion (Section C).

Section A				
Catalyst	T _{10%}	T _{50%}	T _{90%}	
CeO ₂	266	318	387	0.06
Ce _{0.95} Cu _{0.05}	90	113	131	5.62
Ce _{0.85} Cu _{0.15}	85	109	129	7.81
Ce _{0.60} Cu _{0.40}	79	99	117	11.96
Ce _{0.40} Cu _{0.60}	85	111	158	8.03
Ce _{0.15} Cu _{0.85}	115	154	204	1.76
Ce _{0.05} Cu _{0.95}	121	160	194	1.67
CuO	225	249	265	0.45

Section B				
Catalyst	T _{10%}	T _{50%}	T _{90%}	
CeO ₂	410	625	702	0.14
Ce _{0.95} Cu _{0.05}	360	450	525	0.16
Ce _{0.85} Cu _{0.15}	320	418	488	0.42
Ce _{0.60} Cu _{0.40}	280	364	427	8.42
Ce _{0.40} Cu _{0.60}	303	367	418	8.14
Ce _{0.15} Cu _{0.85}	327	399	453	6.26
Ce _{0.05} Cu _{0.95}	324	411	478	2.68
CuO	369	469	562	2.01

Section C				
Catalyst	T _{10%}	T _{50%}	T _{90%}	
CeO ₂	374	440	496	0.19
Ce _{0.95} Cu _{0.05}	329	384	434	0.85
Ce _{0.85} Cu _{0.15}	339	399	458	0.63
Ce _{0.60} Cu _{0.40}	357	427	486	0.27
Ce _{0.40} Cu _{0.60}	352	435	539	0.24
Ce _{0.15} Cu _{0.85}	387	467	532	0.10
Ce _{0.05} Cu _{0.95}	437	479	519	0.03
CuO	434	505	532	0.02

^a Specific CO oxidation rate calculated at 90 °C.

^b Specific C₂H₄ oxidation rate calculated at 310 °C.

^c Specific soot oxidation rate calculated at 350 °C.

due to the easier surface reducibility and more abundant structural defects (oxygen vacancies), as measured by H₂-TPR and micro-Raman spectroscopy (*vide supra*). These findings, are in agreement with the recent studies on the implications of Cu-ceria interactions for the CO oxidation (Table 3). According to the literature [8], the molecule of CO reaches the catalyst surface on Cu-O sites to form CO₂ and then the O vacancy is readily refilled by subsurface (lattice) oxygen.

Conversely, the specific oxidation rates progressively decrease for higher and lower Cu/Ce atomic ratios, while the worst performances can be observed for CuO and CeO₂.

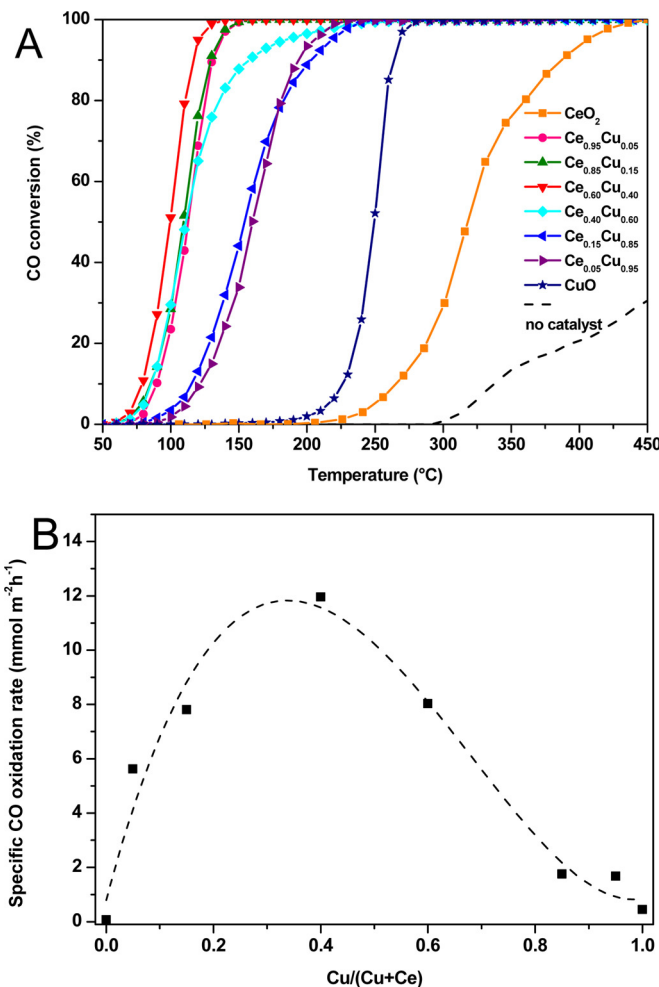


Fig. 8. CO to CO_2 conversion (%) versus temperature (Section A) and specific oxidation rates achieved over the powder catalysts at 90 °C (Section B).

Finally, the CO oxidation activity of the best powder catalyst was studied with the $\text{Ce}_{0.60}\text{Cu}_{0.40}$ -based monolith catalyst. The active phase dispersed on the SiC support revealed the same chemical composition and structural properties of the powder $\text{Ce}_{0.60}\text{Cu}_{0.40}$, as shown in Fig. S1 (Supporting Information). The $\text{Ce}_{0.60}\text{Cu}_{0.40}$ -SiC catalyst has demonstrated good performances, comparable to those obtained with the powder $\text{Ce}_{0.60}\text{Cu}_{0.40}$ ($T_{10\%}-50\%-90\% = 78, 102$ and 133 °C, respectively). Specifically, Fig. 9A shows two catalytic cycles of the catalytic monolith as a function of temperature, for each heating run kept at 450 °C for 1 h. As a result, the catalyst exhibited high stability, and no deactivation occurred for a time-on-stream of 3.5 h at 160 °C (Fig. 9B).

3.3.2. Total oxidation of ethene

The catalytic oxidation of ethene was tested in the 150–700 °C range. Fig. 10A reports the ethylene conversion as a function of temperature: ethene shows no conversion in absence of the catalyst for this temperature range (10% ethene conversion is achieved at 720 °C [62]) and, as expected, the prepared catalysts show positive conversion trends for an increasing of reaction temperature.

However, different conversion trends can be observed: the best specific oxidation activities were achieved for the $\text{Ce}_{0.60}\text{Cu}_{0.40}$ catalyst ($8.42 \text{ mmol m}^{-2} \text{ h}^{-1}$ at 310 °C), thus confirming the beneficial role of the CuO_x clusters interacting with CeO_2 for the total oxidation of ethene. The interaction between the CuO and CeO_2 , indeed, enhances the redox ability of the catalyst that is required to carry on the VOC total oxidation, kinetically modelled via MvK-type mech-

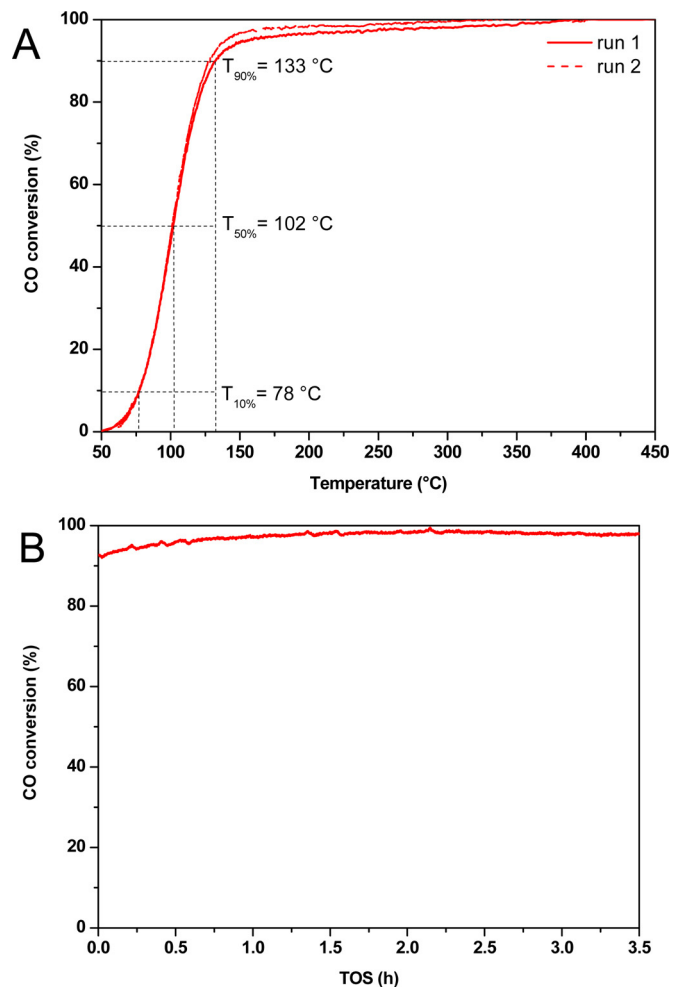


Fig. 9. Stability study of the $\text{Ce}_{0.60}\text{Cu}_{0.40}$ -based monolith catalyst for two successive CO oxidation runs (Section A) and evolution of the CO conversion into CO_2 with time-on-stream on the same catalytic monolith at 160 °C (Section B).

anisms [32–35]. Moreover, it enhances the surface reducibility and promotes the formation of Cu^+ species and structural defects (oxygen vacancies), which accounts for the high VOC oxidation activity over Ce-Cu mixed oxides, in agreement with the recent hypothesis/experimental evidences (Table 3).

The synergistic cooperation between the CuO_x and CeO_x species towards the specific oxidation rates can be observed in Fig. 10B: the synergy reaches maximum values for the binary oxide catalysts having Ce/Cu ratio ranging from 1.5 to 0.67, while the lowest specific activities occur for the CeO_2 and CuO .

Finally, Fig. 11A shows the ethene conversion (%) over the $\text{Ce}_{0.60}\text{Cu}_{0.40}$ -SiC catalyst as a function of the temperature: It appears that the catalytic performances ($T_{10\%} = 330$ °C; $T_{50\%} = 367$ °C; $T_{90\%} = 415$ °C) are similar to those obtained with the powder catalyst (Table 4B). In addition, the catalytic monolith exhibits a good catalytic stability for two successive catalytic cycles up to 700 °C and no significant deactivation phenomena occur for a TOS of 3.5 h at fixed temperature ($T = 430$ °C) (Fig. 11B).

3.3.3. Soot combustion

Fig. 12A shows the soot conversion (%) achieved for the powdered catalysts under “tight” soot-catalyst contact conditions. Unlike the previous gas-solid oxidation reactions, catalysts having $\text{Ce}/\text{Cu} \approx 0.67\text{--}1.5$ (at./at.) displayed worse activity, and the best performing binary oxide catalyst appears the $\text{Ce}_{0.95}\text{Cu}_{0.05}$

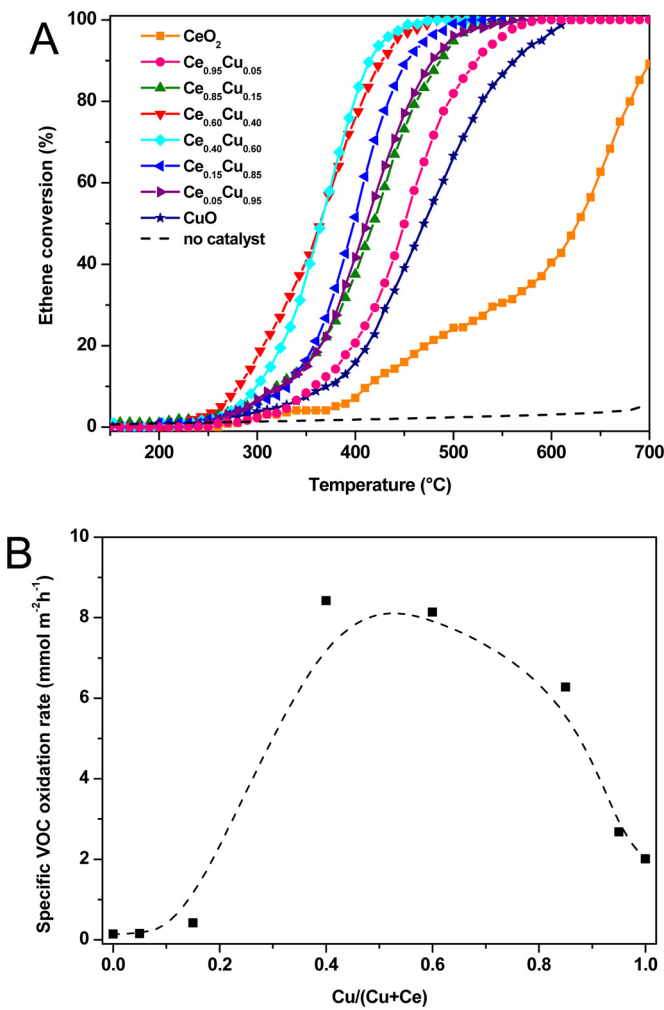


Fig. 10. Total oxidation of ethene as a function of the reaction temperature (Section A) and specific oxidation rates achieved over the powder catalysts at 310 °C (Section B).

($r = 0.85 \text{ mmol g}_{\text{cat}}^{-1} \text{ h}^{-1}$), as shown in Fig. 12B. CO concentrations at the maximum conversion level (measured at T_{peakCO_2}) were above 99% for both binary oxide catalysts and CuO. On the other hand, it was 95.6% for pure CeO_2 (Table S1, Supporting Information).

These findings confirm that the presence of $\text{Cu}^{2+}/\text{Cu}^+$ strongly interacting with ceria framework, as well as the abundance of Cu^+ species, may have a beneficial effect on soot oxidation activity [6,7]. Moreover, the $\text{Ce}_{0.95}\text{Cu}_{0.05}$ sample exhibits a rich population of H-bonded hydroxyl groups (*vide supra*) due the presence of highly reactive Ce-O-Cu species strongly interacting by the SMSI.

The incorporation of Cu species into the ceria framework favors the creation of structural defects (e.g. oxygen vacancies, anion-Frenkel pairs) and then induces the distortion of the oxygen sublattice. On the other hand, the surface density of cerium (a redox active element) decreases as the Cu-content increases. As a consequence, an abundant population of Cu species in the CeO_2 lattice does not have a direct beneficial effect on the soot oxidation activity, since it decreases the surface redox-active centres, which are directly dependent on the surface density of Ce species. In fact, $\text{Ce}^{4+}/\text{Ce}^{3+}$ redox cycles confer the ability to adsorb gaseous O_2 , thus active oxygen (${}^{\bullet}\text{O}_{\text{ads}}$) is formed on the CeO_2 surface, which in turn can be transferred to the soot-catalyst interface by surface diffusion [6].

The best soot oxidation catalyst (namely, $\text{Ce}_{0.95}\text{Cu}_{0.05}$) was used to prepare the catalytic filter (namely, $\text{Ce}_{0.95}\text{Cu}_{0.05}$ -SiC). The chemi-

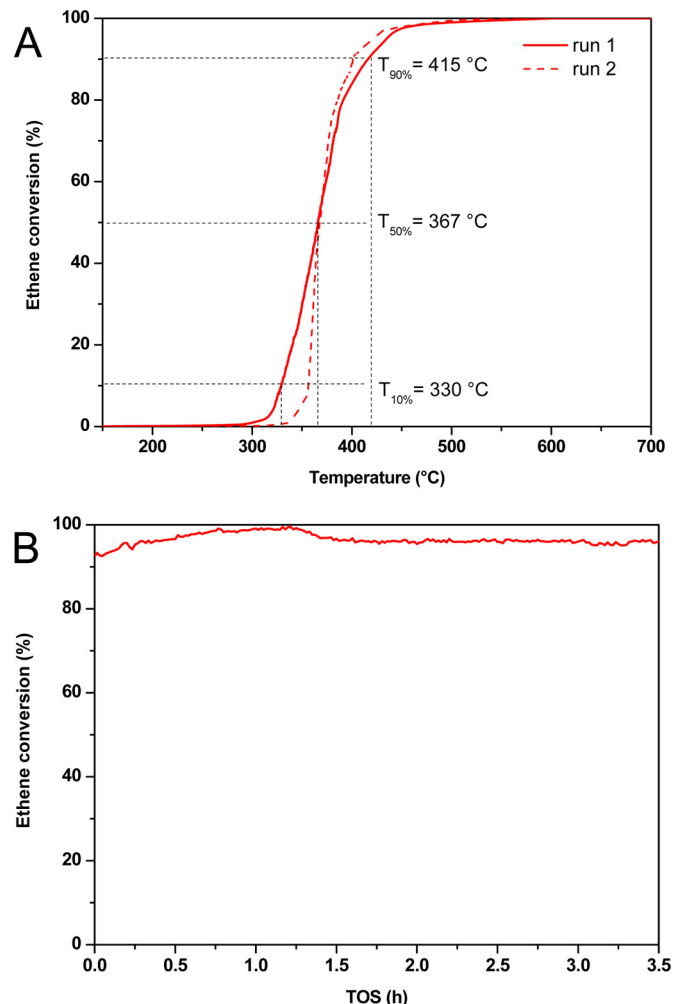


Fig. 11. Stability study of the $\text{Ce}_{0.60}\text{Cu}_{0.40}$ -based monolith catalyst for two successive ethene oxidation runs (Section A) and evolution of the ethene conversion into CO_2 with time-on-stream on the same catalytic monolith at 430 °C (Section B).

cal composition and structural properties of the $\text{Ce}_{0.95}\text{Cu}_{0.05}$ active phase were confirmed by complementary analysis (Fig. S1, Supporting Information).

Fig. 13A shows the soot conversion values (%) achieved over the $\text{Ce}_{0.95}\text{Cu}_{0.05}$ -based monolith filter. As expected, the catalytic performances of the catalyzed filter ($T_{10\%} = 449 \text{ °C}$; $T_{50\%} = 505 \text{ °C}$; $T_{90\%} = 569 \text{ °C}$) are significantly worse than those obtained for the powder $\text{Ce}_{0.95}\text{Cu}_{0.05}$ (Table 4B), because of the different soot-catalyst contact conditions. Indeed, the catalyzed filter was dipped in an organic suspension of soot, whereas the mixture “*powder catalyst + soot*” was prepared by a ball milling to obtain “*tight*” soot-catalyst contact conditions. The latter condition maximizes the soot-catalyst contact points and, although it is less representative of the real contact conditions that occur in a catalytic trap, it is able to discriminate the catalysts better [6]. Many previous studies [6,65], indeed, have shown that the contact conditions between soot and catalyst play a key role in this solid-solid reaction mediated by gas phase oxygen.

Finally, multimodal distributions of CO_2 and CO formations are reported in Fig. 13B and C, respectively. In agreement with the literature [6,65], “peak I” would reflect the CO_x produced via surface redox-type mechanisms, whereas “peak II” can be attributed to CO_x production by radical mechanisms taking place at higher temperatures. The second peak, which is attributed to a nearly uncatalyzed reaction, constitutes only 5% of total soot combustion (Table S2).

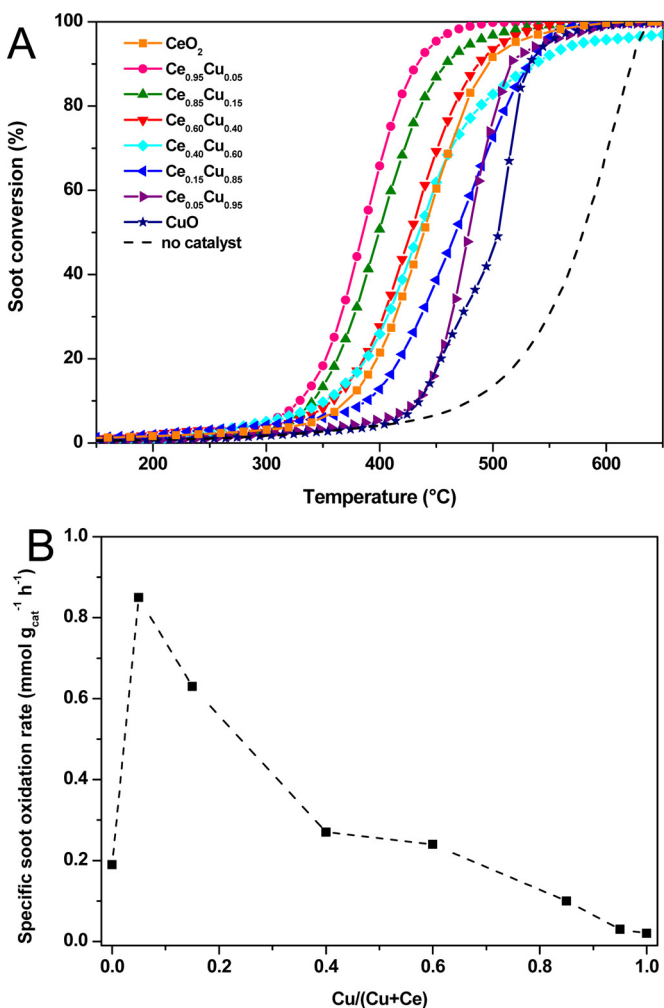


Fig. 12. Soot conversion (%) as a function of the reaction temperature (Section A) and specific oxidation rates achieved over the powder catalysts at 350 °C (Section B).

However, further studies are still necessary to optimize the whole oxidation activity of the catalyzed filter under real operating conditions.

4. Conclusions

A set of binary oxide catalysts with various Ce/Cu contents were synthesized by the solution combustion synthesis (SCS) technique. Catalytic activities of the prepared materials were tested for the CO oxidation, total oxidation of ethene and soot combustion. The best results in terms of both CO oxidation and ethene total oxidation were achieved for the binary oxide catalysts with CeO_x and CuO_x domains that cooperate synergistically during the reaction. Catalysts with CuO_x clusters well dispersed in the CeO_2 appear more active for both the oxidation reactions, probably due to the easier surface reducibility and more abundant structural defects (oxygen vacancies). On the other hand, the soot combustion activity increases as a function of the Ce-content up to 95 at.%, and so the best soot oxidation catalyst exhibits copper highly dispersed into the ceria framework (namely, Ce-O-Cu species), along with an abundant population of Cu^+ species and H-bonded hydroxyl groups. Finally, two monolith catalysts were prepared by the SCS technique and their activity was confirmed in a laboratory-scale pilot plant reactor.

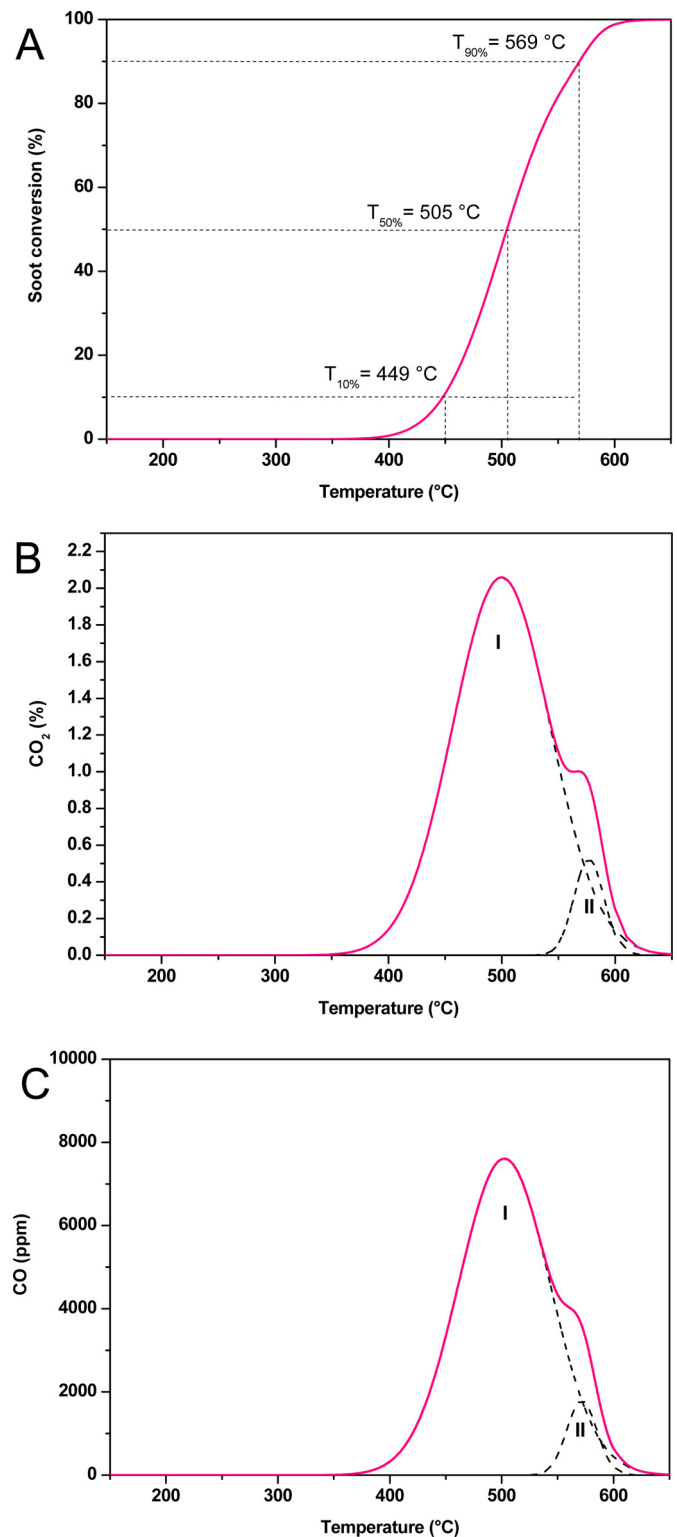


Fig. 13. Soot conversion (%) (Section A) and peaks deconvolution for CO_2 (%) (Section B) and CO (ppm) (Section C) concentration profiles achieved over the $\text{Ce}_{0.95}\text{Cu}_{0.05}$ -based monolith catalyst.

Acknowledgments

The Ministero dell'Università e della Ricerca (MIUR) is acknowledged for sponsoring this research activity (FIRB – Futuro in Ricerca 2012). The Ibiden Co. Ltd. is acknowledged for providing the SiC filters. Authors thank Prof. S. Bordiga and Dr. A. Damin (Università di

Torino, Italy) for Raman measurements, Prof. B. Bonelli and Dr. M. Armandi (Politecnico di Torino) for FT-IR measurements, Prof. G. Martra, Dr. M. Manzoli and Dr. M.C. Valsania for TEM images.

Appendix A. Supplementary data

Supplementary data associated with this article can be found, in the online version, at <http://dx.doi.org/10.1016/j.apcatb.2016.12.054>.

References

- [1] G. Ertl, *Angew. Chem. Int. Ed.* **47** (2008) 3524–3535.
- [2] G. Ertl, H. Knözinger, F. Schüth, J. Weitkamp, *Handbook of Heterogeneous Catalysis*, 2nd ed., Wiley-VCH, Weinheim, 2008, pp. 2394–2411.
- [3] B.K. Hodnett, *Heterogeneous Catalytic Oxidation*, Wiley-VCH, New York, 2000, pp. 189–238.
- [4] S.H. Taylor, *Top. Catal.* **52** (2009) 457.
- [5] W.B. Li, J.X. Wang, H. Gong, *Catal. Today* **148** (2009) 81–87.
- [6] D. Fino, S. Bensaid, M. Piumetti, N. Russo, *Appl. Catal. A* **509** (2016) 75–96.
- [7] M. Piumetti, S. Bensaid, N. Russo, D. Fino, *Appl. Catal. B* **180** (2016) 271–282.
- [8] S. Royer, D. Duprez, *ChemCatChem* **3** (2011) 24–65.
- [9] P. Mars, D. van Krevelen, *Chem. Eng. Sci. Spec. Suppl.* **3** (1954) 41–59.
- [10] J.C. Védrine, G. Coudurier, J.M. Millet, *Catal. Today* **33** (1997) 3–13.
- [11] J.C. Védrine, *Top. Catal.* **21** (2002) 97–106.
- [12] J.C. Védrine, J.M.M. Millet, J.-C. Volta, *Catal. Today* **32** (1996) 115–123.
- [13] M. Piumetti, S. Bensaid, D. Fino, N. Russo, *Appl. Catal. B* **197** (2016) 35–46.
- [14] A. Trovarelli, P. Fornasiero, *Catalysis by Ceria and Related Materials*, 2nd ed., Imperial College Press, London, 2013.
- [15] A. Bueno-López, *Appl. Catal. B* **146** (2014) 1–11.
- [16] J.C. Védrine, *Appl. Catal. A* **474** (2014) 40–50.
- [17] R.A. van Santen, M. Neurock, *Molecular Heterogeneous Catalysis*, Wiley-VCH, Verlag, 2006, pp. 61–62.
- [18] D. Carson, G. Coudurier, M. Forissier, J.C. Védrine, A. Laarif, F. Theobald, *J. Chem. Soc. Faraday Trans. I* **79** (1983) 1921–1929.
- [19] S. Tauster, *Acc. Chem. Res.* **20** (1987) 389–394.
- [20] S.J. Tauster, S.C. Fung, R.L. Garten, *JACS* **100** (1978) 170–175.
- [21] W. Shan, W. Shén, C. Li, *Chem. Mater.* **15** (2003) 4761–4767.
- [22] R.K. Grasselli, *Top. Catal.* **15** (2001) 93–101.
- [23] M. Boudart, *J. Mol. Catal. A* **138** (1999) 319–321.
- [24] W. Curtis Conner, J.L. Falcone, *Chem. Rev.* **95** (1995) 759–788.
- [25] E.M. Gaingeaux, H.M. Abdel Dayem, E. Godard, P. Ruiz, *Appl. Catal. A* **202** (2000) 265–283.
- [26] G.M. Pajonk, *Appl. Catal. A* **202** (2002) 157–169.
- [27] L.-T. Weng, B. Delmon, *Appl. Catal. A* **81** (1992) 141–213.
- [28] G. Avgouropoulos, T. Ioannides, *J. Mol. Catal. A* (2008) 47–53.
- [29] G. Avgouropoulos, T. Ioannides, *Appl. Catal. A* (2003) 155–167.
- [30] M.-F. Luo, Y.-J. Zhong, X.-X. Yuan, X.-M. Zheng, *Appl. Catal. A* (1997) 121–131.
- [31] A. Martínez-Arias, M. Fernández-García, O. Gálvez, J.M. Coronado, J.A. Anderson, J.C. Conesa, J. Soria, G. Munuera, *J. Catal.* **195** (2000) 207–216.
- [32] V. Balcaen, H. Poelman, D. Poelman, G.B. Marin, *J. Catal.* **283** (2011) 75–88.
- [33] D. Delimaris, T. Ioannides, *Appl. Catal. B* **89** (2009) 295–302.
- [34] P.M. Heynderickx, J.W. Thybaut, H. Poelman, D. Poelman, G.B. Marin, *J. Catal.* **272** (2010) 109–120.
- [35] U. Menon, V.V. Galvita, G.B. Marin, *J. Catal.* **283** (2011) 1–9.
- [36] S.L. González-Cortés, F.E. Imbert, *Appl. Catal. A* **452** (2013) 117–131.
- [37] J. Papavasiliou, G. Avgouropoulos, T. Ioannides, *Appl. Catal. B* **66** (2006) 168–174.
- [38] M. Piumetti, S. Bensaid, N. Russo, D. Fino, *Appl. Catal. B* **165** (2015) 742–751.
- [39] J. Ciston, R. Si, J.A. Rodriguez, J.C. Hanson, A. Martínez-Arias, M. Fernández-García, Y. Zhu, *J. Phys. Chem. C* **115** (2011) 13851–13859.
- [40] X. Wang, J.A. Rodriguez, J.C. Hanson, D. Gamarra, M. Martínez-Arias, J. Fernández-García, *Phys. Chem. B* **109** (2005) 19595–19603.
- [41] T. Caputo, L. Lisi, R. Pirone, G. Russo, *Appl. Catal. A* **348** (2008) 42–53.
- [42] P. Bera, K.R. Priolkar, P.R. Sarode, M.S. Hegde, S. Emura, R. Kumashiro, N.P. Lalla, *Chem. Mater.* **14** (2002) 3591–3601.
- [43] J. Wang, D. Tsai, T. Huang, *J. Catal.* **208** (2002) 370–380.
- [44] Z. Wu, M. Li, S.H. Overbury, *J. Catal.* **285** (2012) 61–73.
- [45] W.-W. Wang, P.-P. Du, S.-H. Zou, H.-Y. He, R.-X. Wang, Z. Jin, S. Shi, Y.-Y. Huang, R. Si, Q.-S. Song, C.-J. Jia, C.-H. Yan, *ACS Catal.* **5** (2015) 2088–2099.
- [46] D. Mrabet, A. Abassi, R. Cherizol, T.-O. Do, *Appl. Catal. A* **447–448** (2012) 60–66.
- [47] (a) G. Avgouropoulos, T. Ioannides, *Appl. Catal. A* **244** (2003) 155–167; (b) S. Zhang, W. Huang, X. Qiu, B. Li, X. Zheng, S. Wu, *Catal. Lett.* **80** (2002) 41–46; (c) G.G. Jernigan, G.A. Somorjai, *J. Catal.* **147** (1994) 567–577.
- [48] T. Tabakova, F. Bocuzzi, M. Manzoli, J.W. Sobczak, V. Idakiev, A. Andreeva, *Appl. Catal. A* **298** (2006) 127–143.
- [49] (a) S. Biniak, M. Pakuła, G.S. Szymański, A. Świątkowski, *Langmuir* **15** (1999) 6117–6122; (b) T. Grzybek, J. Klinik, B. Buczek, *Surf. Interface Anal.* **23** (1995) 815–822.
- [50] (a) S. Hocevar, U.O. Krasovec, B. Orel, A.S. Arico, H. Kim, *Appl. Catal. B* **28** (2000) 113–125; (b) A. Tschope, M. Trudeau, J. Ying, *J. Phys. Chem. B* **103** (1999) 8858–8863; (c) L. Kundakovic, M. Flytani-Stephanopoulos, *Appl. Catal. A* **171** (1998) 13–29.
- [51] S. Saikova, S. Vorobyev, M. Likhatski, A. Romanchenko, S. Erenburg, S. Trubina, Y. Mikhlin, *Appl. Surf. Sci.* **258** (2012) 8214–8221.
- [52] S. Suhonen, M. Valden, M. Hietikko, R. Laitinen, A. Savimäki, M. Härkönen, *Appl. Catal. A* **218** (2001) 151–160.
- [53] J.F. Xu, W. Ji, Z.X. Shen, W.S. Li, S.H. Tang, X.R. Ye, D.Z. Jia, X.Q. Xin, *J. Raman Spectrosc.* **30** (1999) 413–415.
- [54] L. Debichi, M.C. Marco de Lucas, J.F. Pierson, P. Krüger, *J. Phys. Chem. C* **116** (2012) 10232–10237.
- [55] W.Y. Hernandez, M.A. Centeno, F. Romero-Sarria, J.A. Odriozola, *J. Phys. Chem. C* **113** (2009) 5629–5635.
- [56] S. Agarwal, X. Zhu, E.J.M. Hensen, L. Lefferts, B.L. Mojet, *J. Phys. Chem. C* **118** (2014) 4131–4142.
- [57] Z. Cheng, B.J. Sherman, C.S. Lo, *J. Chem. Phys.* **138** (2013) 014702-1–014702-12.
- [58] M. Piumetti, M. Armandi, E. Garrone, B. Bonelli, *Microporous Mesoporous Mater.* **164** (2012) 111–119.
- [59] A.A. Davydov, *Infrared Spectroscopy of Adsorbed Species on the Surface of Transition Metal Oxides*, Wiley, Chichester, UK, 1990, pp. 38.
- [60] D. Duprez, F. Cavani, *Handbook of Advanced Methods and Processes in Oxidation Catalysis*, Imperial College Press, London, 2014.
- [61] H.J. Freund, G. Meijer, M. Scheffler, R. Schoggl, M. Wolf, *Angew. Chem. Int. Ed.* **50** (2011) 10064–10094.
- [62] M. Piumetti, D. Fino, N. Russo, *Appl. Catal. B* **163** (2015) 277–287.
- [63] M. Hussain, S. Bensaid, F. Geobaldo, G. Saracco, N. Russo, *Ind. Eng. Chem. Res.* **50** (2011) 2536–2543.
- [64] H. Zhou, Z. Huang, C. Sun, F. Qin, D. Xiong, W. Shen, H. Xu, *Appl. Catal. B* **125** (2012) 492–498.
- [65] M. Piumetti, B. van der Linden, M. Makkee, P. Miceli, D. Fino, N. Russo, S. Bensaid, *Appl. Catal. B* **199** (2016) 96–107.
- [66] M. Konsolakis, *Appl. Catal. B* **198** (2016) 49–66.
- [67] S.D. Senanayake, D. Stacchiola, *Acc. Chem. Res.* **46** (8) (2013).
- [68] H. Bao, Z. Zhang, Q. Hua, W. Huang, *Langmuir* **30** (22) (2014) 6427–6436.
- [69] F. Yang, J. Wei, W. Liu, J. Guo, Y. Yang, J. Mater. Chem. A **2** (16) (2014) 5662.
- [70] H. Yang, Y. Pan, Y. Xu, Y. Yang, G. Sun, *ChemPlusChem* **80** (5) (2015) 886–894.
- [71] T. Umeaki, T. Arai, Y. Kojima, *J. Jpn. Inst. Energy* **93** (12) (2014) 1244–1250.
- [72] S. Sun, D. Mao, J. Yu, Z. Yang, G. Lu, Z. Ma, *Catal. Sci. Technol.* **5** (6) (2015) 3166–3181.
- [73] S. Yao, K. Mudiyanseilage, W. Xu, A.C. Johnston-Peck, J.C. Hanson, T. Wu, D. Stacchiola, J.A. Rodríguez, H. Zhao, K.A. Beyer, K.W. Chapman, P.J. Chupas, A. Martínez-Arias, R. Si, T.B. Bolin, W. Liu, S.D. Senanayake, *ACS Catal.* **4** (6) (2014) 1650–1661.
- [74] J.S. Elias, M. Risch, L. Giordano, A.N. Mansour, Y. Shao-Horn, *J. Am. Chem. Soc.* **136** (49) (2014) 17193–17200.
- [75] Q. Wang, Z. Li, R. Chen, *Chem. Phys. Lett.* **16** (11) (2015) 2415–2423.
- [76] C. He, B.-T. Xu, J.-W. Shi, N.-L. Qiao, Z.-P. Hao, J.-L. Zhao, *Fuel Process. Technol.* **130** (2015) 179–187.
- [77] R. Dziembaj, M. Molenda, M.M. Zaitz, L. Chmielarz, K. Furczon, *Solid State Ionics* **251** (2013) 18–22.
- [78] C. He, Y. Yu, L. Yue, N. Qiao, J. Li, Q. Shen, W. Yu, J. Chen, Z. Hao, *Appl. Catal. B* **147** (2014) 156–166.
- [79] U. Menon, H. Poelman, V. Bliznuk, V.V. Galvita, D. Poelman, G.B. Marin, *J. Catal.* **295** (2012) 91–103.
- [80] X. Zhu, X. Gao, R. Qin, Y. Zeng, R. Qu, C. Zheng, X. Tu, *Appl. Catal. B* **170**–171 (2015) 293–300.
- [81] M. Konsolakis, S.A.C. Carabineiro, P.B. Tavares, J.L. Figueiredo, *J. Hazard. Mater.* **261** (2013) 512–521.
- [82] Y. Wang, J. Wang, H. Chen, M. Yao, Y. Li, *Chem. Eng. Sci.* **135** (2015) 294–300.
- [83] G. Kaur, S. Basu, *Fuel Cells* **14** (6) (2014) 1006–1013.
- [84] H.T. Handal, V. Thangadurai, *Solid State Ionics* **262** (2014) 359–364.
- [85] S. Li, Z. Lu, Z. Yang, X. Chu, Y. Zhang, D. Ma, *Int. J. Hydrogen Energy* **39** (5) (2014) 1957–1966.
- [86] M. Konsolakis, G.E. Marnellos, A. Al Musa, N. Kaklidis, I. Garagounis, V. Kyriakou, A. Al-Musa, N. Kaklidis, I. Garagounis, V. Kyriakou, *Chin. J. Catal.* **36** (4) (2015) 509–516.